



Boiling flow simulations on adaptive octree grids

Mohammad W. Akhtar, Stanley J. Kleis*

Department of Mechanical Engineering, University of Houston, Houston, TX 77204, United States

ARTICLE INFO

Article history:

Received 1 August 2012

Received in revised form 25 January 2013

Accepted 30 January 2013

Available online 6 February 2013

Keywords:

Boiling flows

Octree grids

Volume-of-Fluid

Phase change

Bubble growth rates

Film boiling

AMR efficiency

ABSTRACT

Boiling flow simulations are conducted on adaptive octree grids. A phase change model consistent with the mixture formulation, in conjunction with the Volume-of-Fluid (VOF) model, is used to track the liquid–vapor interface. Test cases including Rayleigh Taylor instability and bubble growth in a uniform superheat are conducted to validate the phase change model on adaptive grids. The validated model is then used to conduct film boiling simulations on both two-dimensional and three-dimensional adaptive grids. The average wall Nusselt number agrees well with the widely accepted correlations of [Berenson \(1961\)](#) and [Klimenko \(1981\)](#) and [Klimenko and Shelepen \(1982\)](#) for film boiling on a horizontal surface. For the test cases presented, the efficiency of the adaptive technique, as measured by the adaptive mesh refinement (AMR) efficiency, is mostly in the range of 50–80%. Although this efficiency is a function of the nature and dimensionality of the problem, this range of efficiency is comparable to those obtained in the simulations of primary jet atomization conducted by [Fuster et al. \(2009\)](#). This work opens the prospect of conducting more realistic (three-dimensional) multi-modal boiling flow simulations, and problems of similar complexity, in an efficient manner.

© 2013 Elsevier Ltd. All rights reserved.

1. Introduction

Liquid–vapor phase change, a fundamental process of boiling and condensation flows, involves the exchange of large amounts of energy in the form of latent heat. This release or absorption of latent heat makes liquid–vapor phase change a key process in many areas from large scale energy generation, to energy storage, to oil refinement in the petroleum industry and cooling of high heat flux electronic devices ([Juric and Tryggvason, 1998](#)). Accurate prediction of heat transfer characteristics is essential from the perspective of successful design as well as for safe operation for the above applications.

The fundamental physical mechanisms involved in boiling exist at small scales, with the underlying phase change process occurring at a very fast rate, and, thus, are not completely understood. Experimental measurements are limited to empirical correlations, for some modes of boiling in particular geometries, generally with a large scatter in computed results ([Juric and Tryggvason, 1998](#)). Direct numerical simulation of boiling flows offers the prospect of providing a better understanding of the dynamic aspects of boiling phenomena.

One of the primary aspects of simulating boiling flows is to accurately predict vapor bubble growth. Early work on the studies of bubble growth involved many simplifying assumptions. Several researchers including [Plesset and Zwick \(1954\)](#), [Mikic et al. \(1970\)](#) and [Prosperetti and Plesset \(1978\)](#) extended the model of inertia

controlled bubble growth of [Rayleigh \(1917\)](#) to include thermal and surface tension effects. One notable contribution to bubble growth analysis has been that of [Mikic et al. \(1970\)](#) who made few simplifying assumptions leading to a more complete description of the bubble growth processes ([Kolev, 2002](#)).

While these results did give some insight into the mechanisms of vapor bubble growth and provide theoretical results to validate numerical simulations, they lack the complete spatial and temporal evolution of the liquid–vapor interface with the associated flow and heat transfer characteristics. Complete numerical simulations of liquid–vapor phase change without the use of ad-hoc models holds the promise to provide greater details of the complicated boiling process.

Early work on advanced simulations of liquid–vapor phase change by [Welch and Wilson \(2000\)](#) involved computation of a fully deformable bubble using moving triangular grids in two dimensions. However, the simulation run time was limited by the amount of grid distortion that could be tolerated. [Son and Dhir \(1997\)](#) simulated film boiling on moving body fitted co-ordinates, but had similar limitations as those of [Welch and Wilson \(2000\)](#). [Juric and Tryggvason \(1998\)](#) and [Son and Dhir \(1998\)](#) presented numerical studies of film boiling, which allowed for large deformations of the interface. [Esmaeeli and Tryggvason \(2004a, 2004b\)](#) presented direct numerical simulations of film boiling on horizontal periodic surfaces. The evolution of interfacial dynamics, heat transfer and fluid flow was studied for different wall superheats.

Direct numerical simulations of nucleate boiling were performed by [Son et al. \(1999\)](#). The growth of a single bubble was modeled by separating the computational domain into macro

* Corresponding author. Tel.: +1 713 743 4536; fax: +1 713 743 4503.

E-mail addresses: mwakhtar3@uh.edu (M.W. Akhtar), kleis@uh.edu (S.J. Kleis).

and microregions. The microregion consisted of the thin liquid film that forms between the bubble and the wall, whereas the macroregion was the fluid domain excluding the microlayer. Lubrication theory was used to model the microlayer dynamics. Computed bubble growth was found to be in agreement with the experimental data, but a proper relation between the heat flux and the wall superheat was not obtained (Shin et al. 2005).

Shin et al. (2005) presented a full direct numerical simulation of nucleate boiling using the Level Contour Reconstruction Method (LCRM), a hybrid approach combining the front tracking and level set methods. Models for the evaporation of the microlayer and contact line dynamics were not included in that study. It was demonstrated that three-dimensional simulations provided better agreement with Nusselt number correlations than the two-dimensional simulations. Also, it was found that the presence of neighboring bubbles is critical to predicting the relationship between heat flux and the wall superheat.

Numerical simulation of fluid flow, including liquid–vapor phase change, is one of the most challenging problems in computational fluid dynamics. Such flows involve discontinuities in material properties (e.g., density, viscosity and thermal conductivity) and flow variables like pressure at the interface. These discontinuities in material properties and flow variables pose additional numerical challenges. For example, multiphase flows in general are accompanied by high density ratios, of the order of 1000, which can degrade solver performance (Popinet, 2009).

Besides solving the Navier–Stokes and the energy equations, an additional task is to track the interface. Interface tracking/capturing methods are broadly classified in the following three groups based on the type of grid and implementation as: (a) deformable volumetric grid to track the interface between the phases, (b) fixed grid approaches where the interface is captured and a volume fraction (VOF method) or a phase indicator or distance function (Level Set) is advected, or (c) Lagrangian approach where a moving grid tracks the interface. Among these schemes, the most commonly employed is the interface capturing on a fixed (non-moving) grid system such as in VOF or Level Set techniques. Also, the robustness and accuracy of the tracking scheme can be improved by using a hybrid approach which combines the strengths of these schemes. The LCRM approach first presented in Shin et al. (2005) was further enhanced with the explicit calculation of a distance function used in the interface reconstruction procedure as well as in the surface tension calculation. Most recently, a hybrid technique, Local Front Reconstruction Method (LRFM), was presented by Shin et al. (2011), where the phase interface is tracked explicitly without the use of logical connectivity leading to automatic topology handling. Improved accuracy and efficiency was obtained in comparison to LCRM, in particular, with respect to local mass conservation. Although hybrid approaches can be used to overcome the limitations of each method, it is to be noted that there are two different representations attempting to represent the same interface leading to additional complexity, efficiency and consistency issues (Popinet, 2009).

While previous investigations have provided insight into the physics of the film boiling process, all of the studies have been done on uniform and non-adaptive grids. It is to be noted that the use of uniform grids, leading to an aspect ratio of unity, is strongly recommended for better accuracy of the reconstruction schemes like that of Rudman (1997), in addition to providing a good quality mesh for the overall flow solution. The use of uniform grids limits the problems scales and the number of boiling modes and their interactions that can be studied, especially in three dimensions. In order to get accurate numerical predictions, the grid has to be fine enough to capture the evolution of the interface while keeping cell aspect ratios close to unity. Previous works of Juric and Tryggvason (1998) and Esmareli and Tryggvason (2004a,b) have used a front-tracking/finite difference technique

to accurately simulate film boiling on a horizontal plate on uniform grids. Welch and Wilson (2000) have presented a VOF technique to simulate film boiling in two dimensions also on uniform grids. While the use of uniform grids may be a feasible approach to present test cases in two and three dimensions, conducting full simulations, in particular multi-mode film boiling in three dimensions on fine uniform grids is too expensive and not practical.

In this work, an interface capturing scheme with phase change on octree grids (adaptive grids) is presented. Here, the grid can be refined locally based on values of variables like interface location or/and gradients of temperature. The VOF method is used with a consistent implementation of the mixture temperature condition at the interface in order to make accurate predictions of heat flux and thus mass generation at the interface. The present results in terms of temporal evolution of the Nusselt number at the wall are shown to compare well with empirical correlations.

A number of test cases are presented to validate and demonstrate the strengths of the numerical technique. In particular, the computational savings and efficiency are compared to uniform grid simulations with the same resolution near the interface. First, the accuracy of the VOF method on octree grids is validated by simulating the test cases of Rayleigh Taylor instability and Enright's deformation test. Also presented are conclusions from the benchmark tests done by other researchers. Next, bubble growth rates under a uniform superheat with zero gravity are compared against the theoretical results of Mikic et al. (1970). This test case validates the phase change model in the absence of gravity in the diffusion dominated regime. Finally, both two-dimensional and full three dimensional simulations of film boiling on a horizontal plate are conducted to demonstrate the capability of the approach. For comparison purposes, the parameters used in this study are within the range of parameters chosen in the studies of Juric and Tryggvason (1998) and Esmareli and Tryggvason (2004b). The results obtained compare very well against widely accepted correlations of Berenson (1961) and Klimenko (1981) and Klimenko and Shelepen (1982) for film boiling on horizontal surfaces in terms of average wall Nusselt number.

2. Mathematical formulation

One motivation for the use of a VOF method is the inherent volume conservation property of this technique. This is particularly important when solving phase change problems. The VOF method, being an implicit formulation (where the interface needs to be reconstructed from the advected volume fraction data), is a single field formulation wherein each fluid variable/property for the phases is represented by a single variable. This single variable, known as a mixture variable, is a linear combination of the variables/properties of each phase weighted by a volume fraction (or mass fraction for energy variables like specific heat). For example, a flow property like density or viscosity for the mixture is written as:

$$P_{mix} = \alpha_l P_l + \alpha_v P_v, \quad (1)$$

where the subscripts *mix* refers to mixture, *l* refers to the liquid phase and *v* refers to the vapor phase.

The single set of conservation equations for mass, momentum and energy in terms of mixture variables is

$$\frac{\partial \rho}{\partial t} + \nabla \cdot (\rho \vec{u}) = 0, \quad (2)$$

$$\frac{\partial (\rho \vec{u})}{\partial t} + \nabla \cdot (\rho \vec{u} \vec{u}) = -\nabla p + \rho \vec{g} + \nabla \cdot \vec{\tau} + \vec{S}_{mom,st} + \vec{S}_{mom,pc}, \quad (3)$$

$$\frac{\partial (\rho c T)}{\partial t} + \nabla \cdot (\rho \vec{u} c T) = -\nabla \cdot \vec{q} + \tau : \nabla \vec{u} + S_{energy}. \quad (4)$$

Here, ρ and c are mixture properties for density and specific heat, \bar{u} is the volume-averaged mixture velocity, T is the mass averaged mixture temperature, p is the volume averaged mixture pressure, and $\bar{\tau}$ is the volume averaged mixture deviatoric stress tensor.

The above equations are derived by Sun and Beckermann (2004) by applying an averaging process to the equations of motion for the individual phases within the interface. In the averaging process, the dispersive flux arising from the average of the non-linear term $\bar{u}\bar{u}$ is neglected. Specifically, the flow inside the interface is assumed to be slow enough to make this assumption valid, which also makes the resulting equations consistent with thermodynamic models. More details involving this assumption and the complete averaging process is detailed by Sun and Beckermann (2004).

The source terms, $\bar{S}_{mom,st}$, $\bar{S}_{mom,pc}$ and S_{energy} , account for surface tension, momentum and energy exchange due to phase change, respectively, on a per unit volume basis between the phases. The heat flux vector is given by $\bar{q} = -k\nabla T$, while $\tau : \nabla \bar{u}$ is the viscous dissipation, a term neglected in the numerical implementation. The source term for momentum due to phase change, $\bar{S}_{mom,pc}$, is specified as $\bar{S}_{mom,pc} = -\dot{m}''\bar{u}$. This source term needs to be included to correctly model the phase change effects on momentum exchange between the phases in FLUENT™ (see Section on Momentum Source Effects in Electronic Annex 1 in the online version of the article). This is because, whenever a mass source is specified in FLUENT™, it automatically adds a corresponding momentum source at the local velocity, which in this case is the mixture velocity at the interface. The effects of surface tension are included in the formulation using the model of Brackbill et al. (1992). This model specifies the surface tension force per unit volume as

$$\bar{S}_{mom,st} = \frac{\rho\sigma\kappa\nabla\alpha_l}{\frac{1}{2}(\rho_l + \rho_v)}, \quad (5)$$

where σ , is the surface tension, κ is the local curvature given by $-\nabla \cdot \bar{n}_l$ and \bar{n}_l is the interface normal defined as $\nabla\alpha_l/|\nabla\alpha_l|$ (Ozkan et al., 2007).

The energy source per unit volume of the cell is defined as

$$S_{energy} = S''_{energy}A_{int}/V_{cell}, \quad (6)$$

where A_{int}/V_{cell} , is the ratio of area of the interface to the volume of the cell and the energy source per unit area of the interface, S''_{energy} , is given by

$$S''_{energy} = -\dot{m}''L = (\bar{q}_v - \bar{q}_l) \cdot \bar{n}_l = (-k_l\nabla T_l + k_v\nabla T_v) \cdot \nabla\alpha_l/|\nabla\alpha_l|. \quad (7)$$

Here, \dot{m}'' is the mass flux (counted as positive from liquid to vapor) per unit area of the interface and L is the latent heat of vaporization at saturation temperature.

2.1. Interface motion

For flows with phase change, the evolution of the vapor (secondary) phase volume fraction is governed by

$$\frac{\partial(\rho_v\alpha_v)}{\partial t} + \nabla \cdot (\rho_v\alpha_v\bar{u}_v) = \dot{m}'' \left(\frac{A_{int}}{V_{cell}} \right). \quad (8)$$

The liquid (primary) phase volume fraction in this case is determined from the volume constraint of a computational cell as

$$\alpha_v + \alpha_l = 1. \quad (9)$$

The above equations give only the discrete volume fraction data. In order to retrieve the interface details, including position and orientation, the interface needs to be reconstructed from the discrete data through the following steps:

(a) First, the interface normal is defined as

$$\bar{n}_l = \nabla\alpha_l/|\nabla\alpha_l|. \quad (10)$$

(b) The interface is then located with a piecewise linear assumption (Piecewise Linear Interface Construction, PLIC) at the calculated orientation such that volume fraction of the phases is correctly represented.

(c) The amount of mass flux through the faces of the computational cell is then obtained from the direction-split approach, as described by Rudman (1997).

2.2. Interface conditions

At the interface, with the assumption of a no-slip condition, the tangential components of the phase velocity are assumed to be everywhere equal to that of the interface, i.e.,

$$\bar{u}_l \cdot \bar{\tau} = \bar{u}_v \cdot \bar{\tau} = \bar{u}_{int} \cdot \bar{\tau}. \quad (11)$$

Here, the subscripts l , v and int refer to liquid, vapor and interface, respectively.

The liquid and vapor temperatures are assumed to be equal to a single interface temperature. This single interface temperature can be assumed to be equal to the saturation temperature at the local liquid system pressure,

$$T_{int} = T_{sat}(P_\infty). \quad (12)$$

This assumption is adequate for most problems. For problems involving a non-flat interface, in particular with high heat fluxes at the interface, a more complete expression for the interface temperature has been presented by Juric and Tryggvason (1998). This interface condition includes the effect of heat fluxes on the interface saturation temperature by including the resistance to mass transfer across the interface. For the test cases presented in this study, the more commonly used expression for interface temperature (Eq. (12)) is used in the numerical implementation.

2.3. Grid generation

GAMBIT™ 2.3.16 (Ansys Inc.) is used to create a uniform parent (base) grid for the test cases. A uniform parent grid is used so that the aspect ratio is unity before and after octree adaption, a criterion essential to the accuracy of the interface reconstruction using the method of Rudman (1997). The grid adaption is conducted every other time step. A schematic of the octree structure and its corresponding tree representation is shown in Fig. 1. The unrefined cell or the parent cell is given an index "0". Each cell, when refined by one level, has four children in two dimensions and eight in three dimensions. The finest or the smallest cell is known as the leaf cell and has no children.

The parent grid is adapted based on refinement criteria specified via user defined functions. The refinement criteria may include regions of steep gradients of flow variables, cells containing or proximal to the interface, interface curvature, and volume fraction gradient. For the test cases investigated in this article, combinations of interface location, proximity to interface, gradient of interface marker and mixture temperature gradient have been explored to refine the parent grid at the required resolution.

A user-defined memory location is used to mark the cells to be refined with the aid of grid adaption functions. After the grid adaption process is completed, the set of user-defined memory locations (total of 32 used for each cell), used to store temporary variables for phase change calculations, is initialized by an additional function to allocate memory for the newly adapted grid. It is to be noted that this is an additional step done through a user-defined function. This grid adaption process is carried out at least

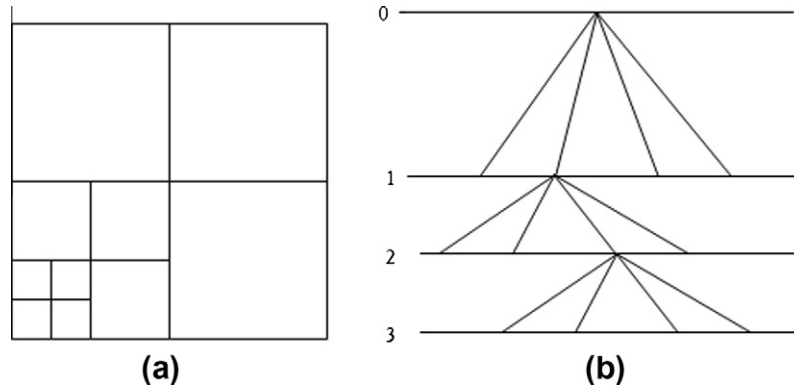


Fig. 1. (a) Octree grid schematic and (b) corresponding tree representation.

every other time step for the test cases presented. In particular, cells containing the interface and two rows of neighboring liquid/vapor cells across the interface width are refined to the finest level. This is done to maintain second order consistent temperature gradient calculations at the faces of the computational cell without the use of special schemes, which would otherwise be required. A more general and probably efficient approach would be to allow for variable resolution along the interface, an attractive scheme for problems involving strong curvature effects. Such algorithms require gradient calculation at fine/coarse boundaries and have been implemented for problems without phase change by Popinet (2009). For test cases presented in this study, the interface cells and two rows of neighboring cells are maintained at the same level of refinement.

2.4. Numerical schemes

The Navier–Stokes and energy equations, in terms of mixture variables, along with the volume fraction equation for the vapor phase, are solved to capture the evolution of the flow field and interfacial dynamics. The fluid dynamics package Ansys FLUENT™ (version 6.3.26) is used to solve these equations on an adaptive octree grid. It is to be noted that the package solves the Navier–Stokes and energy equations and provides the user with source terms to include any additional effects like phase change. The phase change model developed is not a part of the general package and is incorporated with the aid of user defined functions. Also, the grid adaption and memory allocation is controlled through user defined functions.

It was shown by the case studies of Ozkan et al. (2007), that the VOF method of FLUENT™ with geometric reconstruction compares very well with the results obtained using the code TURBIT-VOF, a research code validated against experiments of Thulasidas et al. (1995). Measures like bubble velocity, mean liquid velocity and bubble shape for test cases of co-current bubble-train flow in a square vertical mini-channel, driven by buoyancy only and by buoyancy and external pressure gradient, were used for validation. It was concluded that FLUENT™ gave physically sound and consistent results and was superior to other commercial codes like CFX and STAR-CD for the cases studied.

The set of conservation equations for mass, momentum and energy is solved using the finite volume method. The transport equation for a general scalar, ϕ , in an arbitrary control volume, V , can be written in integral form as

$$\int_V \frac{\partial(\rho\phi)}{\partial t} dV + \oint \rho \phi \vec{u} \cdot d\vec{A} = \oint \Gamma_\phi \nabla \phi \cdot d\vec{A} + \int_V \vec{S}_\phi dV. \quad (13)$$

Here, Γ_ϕ is the diffusion coefficient and S_ϕ is the source per unit volume of the scalar. The integral equation in discretized form is expressed as

$$\frac{\partial(\rho\phi)}{\partial t} V + \sum_f \rho_f \phi_f \vec{u}_f \cdot d\vec{A}_f = \sum_f \Gamma_\phi \nabla \phi_f \cdot d\vec{A}_f + \vec{S}_\phi V, \quad (14)$$

where V is the cell volume and the subscript f indicates the values at the face of the cells. The unsteady term is discretized using a first order Euler scheme.

A co-located arrangement is used to store velocity and pressure at the cell centers. The face values thus require interpolation from the values at the cell centers. The face values needed for the advection term is obtained using the QUICK (Quadratic Upwind Differencing) scheme, a weighted average of the second order upwind and center interpolation of the variable. The diffusion term is discretized using central differences. The face value of pressure is obtained using the PRESTO (pressure staggering option) scheme. Details of the implementation have been provided by Nichita (2010). To obtain the pressure velocity coupling, the PISO scheme of Issa (1986) is used. A flowchart of the PISO algorithm is also provided by Nichita (2010). A point implicit Gauss-Seidel solver in conjunction with the algebraic multi-grid (AMG) method is used to solve the system of equations. The convergence criteria are monitored by scaled residuals. The residual for a general scalar, ϕ , is written as $R^\phi = \sum_{all\ cells} |\sum_{nb} a_{nb} \phi_{nb} + b - a_p \phi_p|$. Here, a_p denotes the influence coefficient at the center, a_{nb} represents the influence coefficient of the neighboring cells and b is the contribution of the constant part of the source term and of the boundary conditions. In general, it might be difficult to judge convergence based on this definition of residuals. FLUENT™ thus, allows for scaling of the residuals with the term $\sum_{all\ cells} |a_p \phi_p|$. For the continuity equation, the residual is defined as $R^c = \sum_{all\ cells} |rate\ of\ mass\ creation\ in\ cell|$. This residual can then be scaled with the largest absolute value of the continuity residual in the first five iterations (Nichita, 2010). As an alternative, FLUENT™ also provides the user a choice of the number of iterations over which the largest absolute residual is determined for use as a scaling factor. The scaled residual limits for continuity, velocities and energy are set to 10^{-4} , 10^{-5} and 10^{-6} , respectively.

2.5. Solution procedure

The solution process starts with an initialization routine which initializes the mixture velocities, pressure and temperature in the entire computational domain and the initial location of the interface. A set of user-defined memory locations are used to keep track of the interface and neighboring cells for grid adaption, and to store liquid and vapor temperature gradients along with some other intermediate values like the area of interface to cell volume ratio. An on-demand function is called at the beginning of each time step to set the memory location pointers after the grid has been updated. Next, an adjust function is called which marks the interface

and two sets of neighboring cells, both on the liquid and vapor sides of the interface, for grid adaption to the finest level. This function also marks the cells to be used in the calculation of the liquid and vapor temperature gradients. A second adjust function is then called that calculates the heat flux into the interface, sets the temperature condition in the interface cells, and calculates the area of interface to cell volume ratio. The mass source is then estimated from the energy source and the latent heat on a per volume basis (Eqs. (6) and (7)) and stored in a memory location for each cell for estimating the mass, momentum and energy exchange between the phases. Finally, the source functions for liquid mass, vapor mass, mixture momentum and energy are called, which calculate the values for each cell to be returned to FLUENT™. Complete details of the phase change model are provided in Akhtar (2011).

2.6. Time step restrictions

The magnitude of the allowable time step for stable calculations is determined from the surface tension, convective and viscous terms. The surface tension (capillary) constraint is given by $\Delta t = \sqrt{\frac{\rho_l + \rho_v}{4\pi\sigma}} \min(\Delta^3)$, the convective constraint is given by $\max(\frac{|\vec{u}|\Delta t}{\Delta}) < \text{CFL}$ and the viscous constraint is given by $\Delta t < \min\left[\left(\frac{\rho}{\mu}\right)\left(\frac{\Delta^2}{6}\right)\right]$ (Zakerzadeh, 2008). Here, Δ is the mesh size, Δt is the time step and CFL is the Courant–Friedrichs–Lewy condition. For the convective constraint, the CFL is chosen so that for a given time step, the fluid volume advected into the neighboring cell is no more than the volume existing in the cell before advection. The default value of CFL in FLUENT™ is 0.25. Other VOF codes have used a CFL value of 0.5 (Zakerzadeh, 2008).

2.7. Interface temperature condition

A mixture temperature condition is specified in the cells containing the interface. This temperature condition maintains the (effective) interface at the saturation condition in order to estimate the heat flux from both the liquid and vapor sides into the interface. With the use of mixture temperature gradient, interface normal, cell width, and mixture properties, the cell mixture temperature for the interface cells are calculated such that the internal energy is balanced as if the interface were sharp and at the local saturation temperature. The interface is thus at saturation even though the liquid and vapor proximal to the interface may be above saturation. This mixture temperature condition is evaluated and imposed as a thermal condition every time step.

2.8. Computational efficiency

The octree structure allows for local refinement resulting in significant computational cost savings, especially for problems with large variation in spatial scales. Instead of just comparing the savings of computational time when using an adaptive grid for similar accuracy as the uniform grid, the adaptive mesh refinement (AMR) efficiency is computed. The AMR efficiency is defined as

$$\eta_{\text{AMR}} = \frac{t_{\text{uniform}}/\text{Size}_{\text{uniform}}}{t_{\text{AMR}}/\text{Size}_{\text{AMR}}} \quad (15)$$

Here, t denotes the time taken for a given grid *Size* (total number of cells) with subscripts *uniform* and AMR referring to uniform, and adaptive mesh refinement, respectively. This measure of efficiency has been used by Fuster et al. (2009). As noted by Fuster et al. (2009), the efficiency of AMR is quite specific to the nature and dimensionality of the problem. The AMR efficiency was found to be about 61% for the two-dimensional simulations and as high as 95% for a 3D example of the study of instabilities produced in primary

atomization presented by Fuster et al. (2009). For the two-dimensional film boiling example in this work, the AMR efficiency is about 52%. By definition, a higher AMR efficiency would generally occur for larger simulation domains and for higher resolution. For complex problems like 3D film boiling, the use of AMR is very helpful in order to obtain accurate results within a reasonable computational time.

3. Results

Before demonstrating the capability of the phase change model to simulate film boiling, the performances of the interface capturing scheme and the phase change model are evaluated using the test cases of FLUENT™ Verification (Other Investigations), Momentum Source Effects, Rayleigh–Taylor instability, Enright’s deformation test case, parasitic currents test case, and diffusion controlled bubble growth in a uniform superheat. Savings in computational time and AMR efficiency are also assessed, when possible. For the verification test cases results of FLUENT™ Verification (Other Investigations), Momentum Source Effects, Rayleigh–Taylor instability and Enright’s deformation test, see Electronic Annex 1 in the online version of this article.

3.1. Parasitic currents

The problem of a curved interface to remain at rest in the presence of surface tension forces, with only the pressure jump across the interface is often used to determine the accuracy of the numerical model of surface tension. The numerical scheme to estimate the surface tension force and the pressure gradient in general may not be accurate and/or consistent and can lead to what is generally referred to as spurious or “parasitic” currents near the interface. For the test cases presented in this study, reducing the effect of parasitic currents is not actively sought after, but the magnitude of these currents is evaluated. In addition, the current phase change model is intended more for applications in the study of problems like “sliding bubbles”, in which the fluids used in other experimental/numerical studies are mostly refrigerants. In particular, we intend to simulate FC-87 bubbles sliding against a heated inclined wall under the effects of buoyancy forces. Refrigerants belonging to the class of FC-87 have a low value of surface tension ($\sim 1/8$ th of that of an air–water system). In addition, such bubbles are relatively large, with radii ~ 1 mm, and thus, surface tension effects are expected to be small.

In one of the earlier implementations of Shin and Juric (2002), parasitic currents have been measured by the capillary number, i.e., $Ca = U_{\text{max}}\mu/\sigma$, where U_{max} is the maximum velocity in the domain for different Laplace numbers given by $La = \sigma\rho D/\mu^2$. In the front tracking method presented by Tryggvason et al. (2001), for a drop of radius 0.25 in a 1×1 domain resolved by 25^2 grid, the parasitic currents as measured by Ca were found to be order of 10^{-4} for a La of 250. The model of Shin and Juric (2002), for this same test case gives Ca number of the order of a maximum of 10^{-3} with reconstruction and $O(10^{-4})$ without reconstruction. Reconstruction in the model of Shin and Juric (2002) is performed as a way to collect the elements that are physically linked to handle interface merging and break up. The required element operations (deletion, addition, reconnection) can be achieved simultaneously in one step through the reconstruction method as prescribed by Shin and Juric (2002).

A square domain of size (1×1) with a bubble of radius 0.25 in a 30^2 grid was chosen to study the effect of parasitic currents in the FLUENT™ solver. For a La number of 250, the magnitude of the parasitic currents based on the maximum velocity, as measured by the Ca is $O(10^{-3})$. While this magnitude of parasitic currents is small but not negligible, the order is comparable to the model of Shin and Juric (2002) with reconstruction.

A more recent investigation of Shin and Juric (2009) presents a hybrid interface method based on front tracking and level set methods. In particular, a compact curvature field for the computation of the surface tension force is formulated showing improved accuracy in the implementation of the surface tension force. A drop of radius 0.25 in a $1 \times 1 \times 1$ box on a $20 \times 20 \times 20$ grid is used to assess the magnitude of parasitic currents. The La number based on liquid (water) properties is 5×10^5 and based on gas (air) properties is 5×10^6 . For this test case, the maximum spurious velocity is found to be of the $O(10^{-3})$ for the hybrid surface tension model and of the $O(10^{-4})$ for the compact surface tension model for a run of 50 time units.

Using the current scheme, a test case of a static FC-87 bubble of radius 0.25 in its liquid phase is conducted on a 30×30 grid. The La number based on liquid properties is 37.4×10^6 and is 40.9×10^7 based on the vapor properties. The magnitude of the maximum spurious velocity is shown in Fig. 2 and is seen to be of the $O(10^{-3})$. For this test case, the maximum spurious velocity is similar to the hybrid surface tension model but higher than the compact surface tension model of Shin and Juric (2009). The maximum spurious velocity, though small, is not negligible, but the interface does not become unstable.

Although the continuum-surface-force (CSF) is known to suffer from parasitic currents, for the case of a stationary droplet in equilibrium, it has been noted by Renardy and Renardy (2002) and Francois et al. (2006), that it is possible to recover exact discrete equilibrium provided (a) the discrete gradient operators of pressure and volume fraction are compatible and (b) the estimated curvature is constant. This has been shown to be the case with the implementation of height-function curvature estimation with the VOF method by Popinet (2009). The investigation of Popinet (2009) also provides a more clear demonstration of the origin of the so called “spurious currents” and their temporal evolution. These “spurious currents” were shown to be velocity fluctuations, as the result of a physically-consistent numerical solution of a perturbed initial interface, which are damped exponentially on the order of the viscous timescale. On the contrary, these “spurious currents” have been mostly recognized and described as non-physical currents that do not reduce with time and are unrelated to capillary waves (Popinet, 2009). While negligible “parasitic currents” were shown for the case of static droplet under equilibrium, with Popinet’s method, such configurations are not a practical test case. Droplets or bubbles in general do not stand still but move under the effects of external forces like buoyancy. A more realistic test case constructed by Popinet (2009) is the case of a droplet translating in a uniform flow with surface tension. Unlike the results of the static droplet case, the velocity does not converge toward the exact solution with time and the maximum errors in velocity are of the order of 5% of the translating velocity. This test case, first presented by Popinet (2009), is a test of the combined accuracy of the advection scheme, curvature estimation and the surface tension scheme. Thus, further advances are needed to properly address the issue of “parasitic” currents for more realistic examples.

3.2. Bubble growth rates with uniform superheat

Vapor bubble growth rates in liquid FC-87 with a uniform superheat of 5°C in the absence of gravity is validated against the predictions of Mikic et al. (1970). The bubble, initialized at an initial radius of 1 mm in a cubic domain of size 12 mm, is simulated to grow to twice its initial size. Only half of the bubble is simulated exploiting symmetry, while the rest of the domain boundaries are specified with a pressure outlet condition (the static pressure is specified to be atmospheric with a temperature condition equal to the liquid superheat).

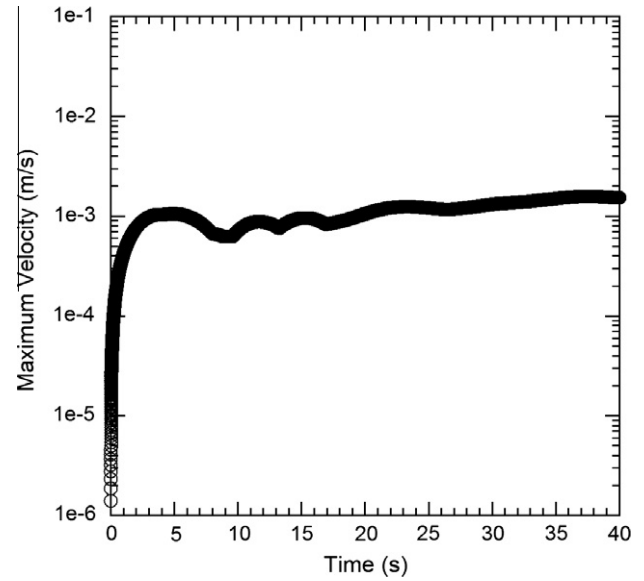


Fig. 2. Maximum spurious velocity for a bubble of radius 0.25 on a 30×30 grid (La for liquid = 37.4×10^6 ; La for vapor phase = 40.9×10^7).

As pointed out by Koley (2002), the analysis of Mikic et al. (1970) is considered to be the most successful compromise between strict formulation and simplifying assumptions and, thus, is chosen to validate the simulated growth rates. The growth rate comparison is done in the dimensionless co-ordinates of bubble radius and time defined as

$$R^+ = \frac{R}{B^2/A}, \quad t^+ = \frac{t}{B^2/A^2}, \quad (16)$$

where $A = \left(\frac{2\Delta T L \rho_v}{3T_{sat} \rho_l}\right)^{1/2}$ and $B = \left(\frac{12}{\pi} \alpha_l\right)^{1/2} Ja$. The Jakob number, Ja , is defined as

$$Ja = \frac{\rho_l c_l \Delta T}{\rho_v L}, \quad (17)$$

where the temperature difference ΔT is the bulk liquid superheat.

A comparison of the computed growth rate curve to the theoretical solution of Mikic et al. (1970) is shown in Fig. 3. Since the simulation is started from a non-zero initial radius, the simulation time is advanced by the time of the theoretical solution corresponding to the initial radius of 1 mm. As can be seen from the figure, the simulated growth rates correspond to the diffusion controlled regime of the Mikic solution. The different regimes are shown in order to better understand the region where the simulated growth lies in the life of a nucleating bubble. The test cases presented in this study involve the growth of larger bubbles, which do not fall in the inertial growth regime. The bubble growth model evaluation is thus limited to the diffusion controlled regime.

To better compare the simulated growth rates against the diffusion limit and to check grid convergence, growth rates are plotted for $t^+ > 10^5$ in Fig. 4. As is seen from the figure, the agreement between simulations and theory is excellent. This theoretical solution of Mikic et al. (1970) has been shown to be in good agreement with the experimental data of Florschuetz et al. (1969) ($\Delta T = 3.61^\circ\text{C}$, system pressure 1 atm, $Ja = 10.77$), and Dergarabedian (1960) ($\Delta T = 6.4^\circ\text{C}$, system pressure 1 atm, $Ja = 9.2$), for this range of superheats and Ja in the study conducted by Lee and Merte (1996).

The temperature field near the interface is initialized at the initial radius consistent with the theoretical solution. This avoids the artificially steep initial temperature gradient, which is a function of grid size. A mass balance at the interface gives

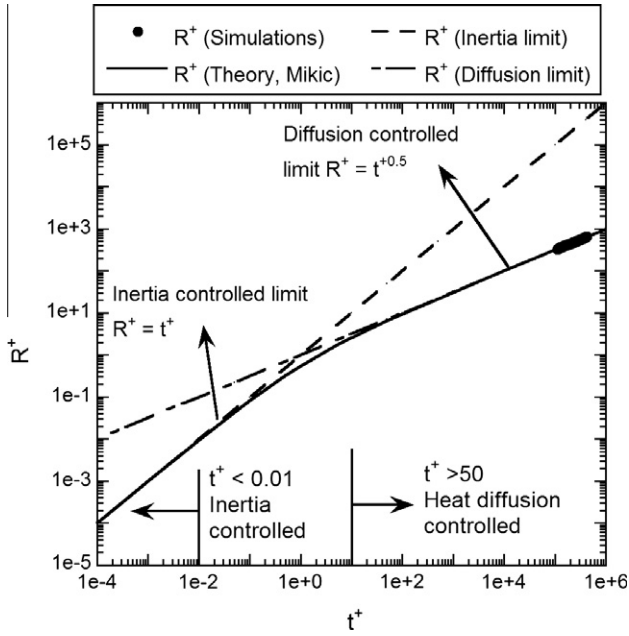


Fig. 3. Comparison of growth rates: Theory, Mikic et al. (1970); inertial and diffusion limits (adapted from Lee and Merte (1996)) and simulated (superheat = 5 °C, $Ja = 8.6$).

$$\dot{m}''(4\pi R^2) = \rho_v \frac{d}{dt}(4\pi R^3) = -\frac{k_l}{L}(\vec{\nabla}T \cdot \vec{n}) = -\frac{k_l}{L} \frac{dT}{dr}. \quad (18)$$

Using the theoretical solution of Mikic et al., the radial temperature gradient can be written as

$$\frac{\partial T}{\partial r} = -\frac{L\rho_v}{2k_l} \left(\frac{A}{(t^*)^{1/2}} \right) = -\frac{L\rho_v}{2k_l} \left(\frac{B^2}{R} \right). \quad (19)$$

On further simplification, the initial radial temperature gradient is expressed as a function of initial radius, uniform superheat, and the Jakob number by

$$\frac{\partial T}{\partial r} = -\frac{6}{\pi} \left(\frac{Ja\Delta T}{R_i} \right). \quad (20)$$

Since Ja depends upon ΔT , the initial temperature gradient thickness is proportional to ΔT^2 . This equation is used to initialize the temperature field for different grid sizes considered in order to conduct proper convergence studies. The bubble is initialized at the saturation temperature, while the liquid beyond the gradient region is initialized at a uniform superheat of 5 °C and 3.5 °C.

Grid convergence is also shown in Fig. 4, by comparing the simulated growth rates for uniform superheats (SH) of 5 °C and 3.5 °C. A superheat value of 3.5 °C gives an initial temperature gradient that is twice as thick when compared to the 5 °C superheat. Bubble growth rates are shown for a superheat of 5 °C on a grid with a parent cell size of 400 μm with 1, 2 and 3 maximum levels of refinement (corresponding leaf cell size = 200 μm , 100 μm and 50 μm). Also, shown are bubble growth rates for a uniform superheat of 3.5 °C on the same parent grid with 1 and 2 levels of maximum refinement (corresponding leaf cell size = 200 μm and 100 μm). The 100 μm (2 levels of refinement), 3.5 °C solution and the 50 μm (3 levels of refinement), 5 °C case agree very well with the theoretical solution. Also, the 200 μm (1 levels of refinement), 3.5 °C solution and the 100 μm (2 levels of refinement), 5 °C case have very similar asymptotic slopes, although both of the cases are different from the theoretical solution. These comparisons clearly show that the growth rate solutions depict convergence

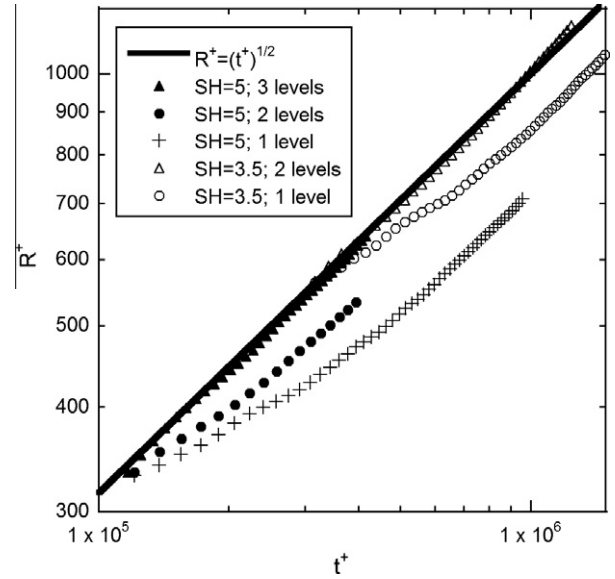


Fig. 4. Comparison of theoretical and simulated growth rates (superheat, SH = 5 °C and 3.5 °C, 1% of points shown for clarity).

for the finer grids. A more detailed and complete verification of the convergence has been presented in Akhtar (2011).

It is to be noted that the initial temperature gradient given by Eq. (20) is a function of R_i and ΔT^2 . For the grid convergence studies, ΔT is chosen such that the temperature gradient differs by a factor of two for the two solutions (5 °C and 3.5 °C solutions) while keeping the bubble initial radius the same. This means that the grid resolution for the 5 °C, 3 levels of refinement and 3.5 °C, 2 levels of refinement would be the same relative to the gradient thickness. Another choice could be to use the same initial R^* for the two cases. One possible combination is to use 5 °C solution with $R_i = 1$ mm and 3.5 °C solution with R_i as 0.59 mm. But, this choice would lead to a ratio of temperature gradient thickness of 1.2, which would be difficult to compare for convergence studies.

In order to compare the performance of the adaptive grid vs. the uniform grid, bubble growth rates are computed on a uniform grid size of 50 μm (domain size: 4 mm \times 4 mm \times 2 mm) and on an adaptive grid of parent cell size of 400 μm and maximum level of

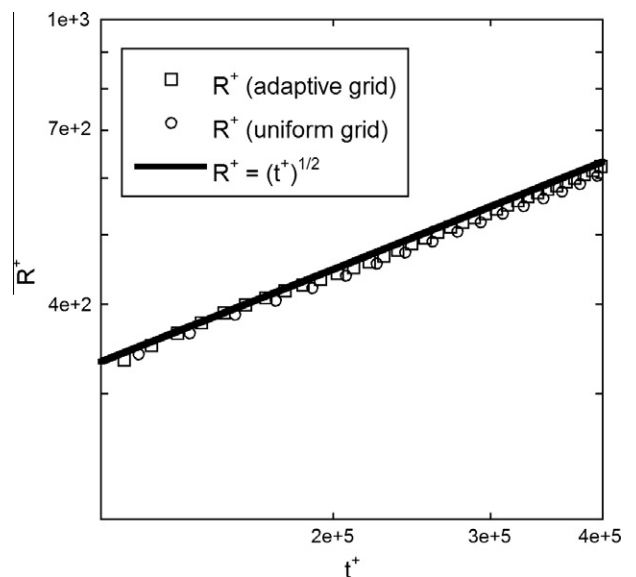


Fig. 5. Growth rates with adaptive grid (three levels of refinement, leaf size = 50 μm) and a uniform grid (size = 50 μm); 1% data points shown for clarity.

Table 1

Comparison of the performance of uniform vs. adaptive grid for the bubble growth test case.

| Parent grid size | Refinement level | Total number of cells (0.2 s) | Simulation time (s) | AMR Efficiency (%) |
|------------------|------------------|-------------------------------|---------------------|--------------------|
| 80 × 80 × 40 | 0 | 256,000 | 103,014 | – |
| 10 × 10 × 5 | 3 | 65,075 | 33,009 | 79.3 |

refinement of 3 (domain size: 4 mm × 4 mm × 2 mm). The computed growth rates for the adaptive grid match very well to that of the uniform grid, as shown in Fig. 5, verifying the accuracy of the adaptive grid implementation. The performance of the adaptive grid is listed in Table 1, which gives an efficiency of 79.3%. It is to be noted that when using adaptive grids the problem size is significantly reduced and thus does not require large amounts of memory allocation. This is an attractive feature making it feasible to run such simulations, with wide range of problem scales, on desktop computers.

3.3. Film boiling

In this section, film boiling simulations on horizontal periodic surfaces are presented. In film boiling, a vapor film completely covers the heated surface. Denser liquid above the vapor film falls under the action of gravity resulting in Rayleigh–Taylor instability. As part of the liquid–vapor interface rises away from the heated wall, other parts of the interface move towards the wall. As the liquid moves closer to the wall, evaporation at the liquid–vapor interface prevents the liquid from getting in contact with the wall. Vapor generation at this and other parts of the interface feeds the mushroom shaped rising vapor jet. As the mushroom shaped vapor region grows in size, the vapor stem pinches off at some point leading to release of the vapor bubble. Thereafter, a new vapor mushroom forms, and the process repeats itself. This sequence of events leads to a quasi-steady state process of vapor generation, vapor break off and finally removal of vapor bubbles while maintaining a complete vapor blanket on the heated surface.

The parameters that characterize film boiling are the thermo-physical properties of liquid and vapor phases (density, viscosity, thermal conductivity and specific heat), the force of buoyancy, interfacial properties like surface tension and latent heat of vaporization, and the thermal input/driver specified in terms of the wall superheat or the wall heat flux. Non-dimensional groups of these parameters are: Grashof no., $Gr = \rho_v(\rho_l - \rho_v)g l_s^3 / \mu_v^2$, which represents the ratio of buoyancy to viscous force; Jakob no., which represents the ratio of sensible heat to latent heat, defined as $Ja = c_v \Delta T / h_{fg}$ or $q_w / \rho_g u_s h_{fg}$ depending on whether the vapor superheat or wall heat flux is specified; Morton no., $Mo = \mu_l^4 g / \sigma^3 \rho_l$; and Prandtl no., $Pr_v = \mu_v c_{p,v} / k_v$, defined as the ratio of momentum to thermal diffusivity for the vapor phase. These non-dimensional groups use $l_s = \sqrt{\sigma / (\rho_l - \rho_v)g}$ as the capillary length scale, $u_s = \sqrt{l_s g}$ as the velocity scale and $t_s = \sqrt{l_s / g}$ as the time scale for the problem.

In order to have a complete set of properties to have a unique boiling configuration, the ratio of material properties like density, viscosity, thermal conductivity, and specific heat are also specified. Table 2 gives the set of parameters used for the film boiling simulations. This set of thermo-physical properties are close to those of saturated water at $p_{sat} = 169$ bar except for the Grashof number, Gr , which is 17.93 for this test case. This choice of properties is very similar to those used for the validation of the numerical method, developed by Esmaeeli and Tryggvason (2004a) to compute boiling flows. The choice of a lower Grashof number, implying a more viscous fluid, and would not require resolving an extremely thin vapor film on the wall. In a subsequent investigation of film

Table 2

Thermo-physical properties of fluid used in test cases.

| T_{sat} | ρ_l / ρ_v | μ_l / μ_v | k_l / k_v | c_l / c_v | Pr_v | Gr | Ja | Mo |
|-----------|-------------------|-----------------|-------------|-------------|--------|-------|-------|-----------------------|
| 625 | 4.78 | 2.59 | 3.56 | 0.66 | 4.39 | 17.93 | 0.071 | 7.69×10^{-3} |

Table 3

Length, time and velocity scales and most unstable wavelength for the film boiling example.

| l_s | t_s | u_s | λ_c | λ_{d2} | λ_{d3} |
|-------|-------|-------|-------------|----------------|----------------|
| 0.103 | 0.1 | 1.0 | 0.64 | 1.12 | 1.58 |

boiling, Esmaeeli and Tryggvason (2004b) showed that the major observations made in their study with low Grashof number flows, for two dimensional systems, carried over to flows with higher Grashof numbers. In the present investigations, the focus is kept on the presentation of a numerical technique, with test cases to validate the methodology, with particular emphasis on adaptive grids to reduce overall computational cost. Thus, the test cases mostly comprise of flows with lower Grashof numbers. The effects of these important non-dimensional numbers are certainly of interest to understand their effects on the physics of film boiling, and we expect to investigate this more in a future study.

With this choice of fluid properties, the length, velocity and time scales and the most unstable wavelengths for the problem are as listed in Table 3. Here, $\lambda_c = 2\pi l_s$ is the critical Taylor wavelength and λ_{d2} is the most unstable Taylor wavelength in two dimensions given by $\lambda_{d2} = 2\pi\sqrt{3}l_s$. For the case of film boiling on a horizontal surface, Lao et al. (1970) showed that λ_{d3} ($\lambda_{d3} = \sqrt{2}\lambda_{d2}$) is the most unstable Taylor wavelength in three dimensions.

Next, a two-dimensional domain is used to demonstrate the capability of the method to simulate film boiling and to show the improvement of computational efficiency in comparison to uniform mesh for the same accuracy. Also, the two-dimensional simulations are used to study the convergence behavior of the method both in space and time. Finally, a test case is presented in full three dimensions to demonstrate the robustness of the method and its applicability for further studies of film boiling and other problems of similar complexity.

A rectangular domain of size approximately ($\lambda_{d2}, 3.6\lambda_{d2}$) is chosen for the study. A heavier fluid of density 1.225 kg/m³ lies above a lighter fluid of density 0.256 kg/m³. The relevant properties/parameters are listed in Table 2. The interface between the fluids is given an initial perturbation with the vertical position given as $y = y_c + A \cos(2\pi n_x / W)$. Here, the unperturbed height of the interface (y_c) and the amplitude of the cosine wave (A) are chosen to be $0.125\lambda_{d2}$ and $0.05\lambda_{d2}$, respectively. The remaining parameters are W , which is the domain width, and n_x being the number of modes of the perturbation chosen as 1. Fig. 6 shows the contours of mixture temperature at times 0 and 1.0 s (sub-figures (a) and (b)) and contours of vertical velocity at 1.0 s. The interface location is shown by the black line. A linear temperature profile is imposed from saturation temperature at the domain top boundary (625 K) to a superheated wall (640 K) at the bottom. Due to the initial interface perturbation, a hydrostatic pressure difference exists between the crest and troughs of the interface.

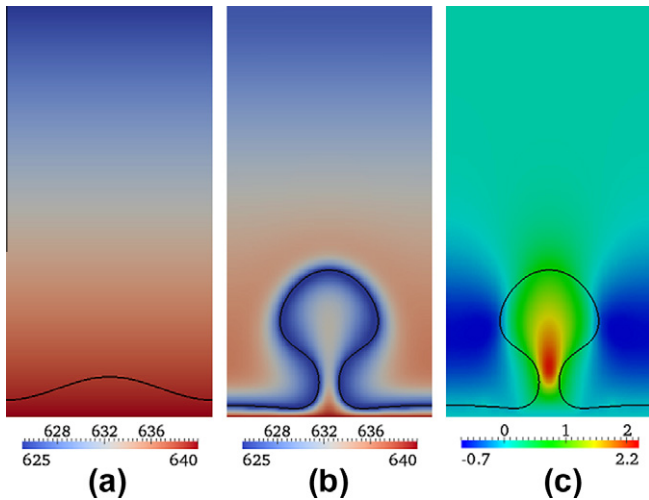


Fig. 6. Film boiling: Contours of mixture temperature at times (a) 0 s (single mode perturbation), (b) 1.0 s and (c) contours of vertical velocity at 1.0 s (interface location has been superimposed as black line). The fluid properties used correspond to the ones listed in Table 2.

This pressure difference results in liquid moving downward toward the wall in the troughs and vapor rising at the crest. As a result, the vapor moves towards the crest growing into a mushroom shaped bubble with the additional aid of vapor generation due to the heat flux pumped into the interface from the superheated wall. Two counter-rotating vortices are formed on either side of the mushroom peak as indicated by the velocity plot in Fig. 6c. The plunging of the liquid at the interface trough is accompanied by a steeper temperature gradient at the interface resulting in more vapor generation and preventing the liquid from wetting the superheated wall.

A detailed grid convergence study was carried out to show the consistency and thus convergence of the numerical scheme in both space and time. Once the convergence of the numerical scheme was established, adaptive grid solutions were computed to demonstrate computational savings.

Fig. 7 shows the iso-surface of 0.5 volume fraction on (a) uniform grids of size 32×64 (white), 64×128 (dashed gray) and 128×256 (solid black) at 1.0 s. The interface shape is very similar between the three cases. In order to get a better measure of grid convergence, the vapor volume and the wall Nusselt number are compared for the grids chosen. The space averaged Nusselt number is defined as $Nu_{avg} = -l_s / (A\Delta T) \iint \partial T / \partial y|_w dA$. As can be seen from Table 4, the difference in the vapor volume and the Nusselt number between the 64×128 and 128×256 cases is only 0.8% and 6.4%, respectively. The 128×256 grid solution can thus be considered as a converged solution (independent of the mesh size).

Two adaptive grids are also used, namely a 32×64 grid with 2 levels of maximum refinement and a 64×128 grid with 1 level of maximum refinement. The cells containing the interface and two rows of cells next to the interface on either side are refined to the maximum level. Thus, the interface and the neighboring cells have the same cell size between the two adaptive grids and the uniform grid of size 128×256 . The interface heat fluxes for the adaptive grids are thus resolved to a similar accuracy as the uniform grid. The refinement process was carried out every other time step. The interface shapes using these adaptive grids is compared against the finest uniform grid of resolution 128×256 in Fig. 7b. As can be seen from the figure, the interface shapes on adaptive grids (gray and white contour) are very similar to the one on the uniform grid (solid black). Also, it is seen from Table 4 that both the vapor volume and Nusselt number for the adaptive grids are

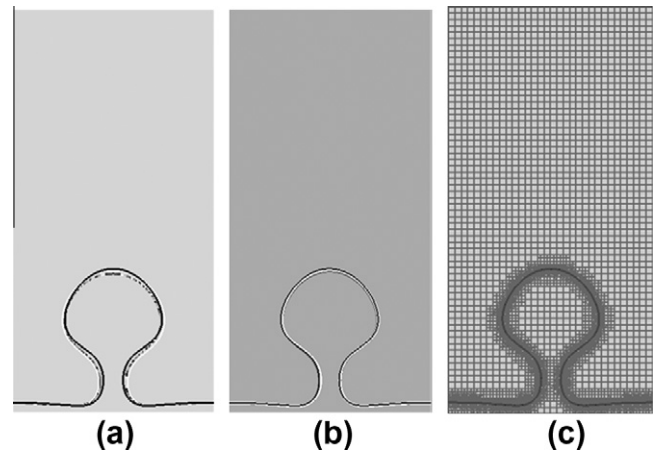


Fig. 7. Film boiling: (a) Iso-surface of vapor volume fraction = 0.5 on (a) uniform grids of size 32×64 (white), 64×128 (dashed gray) and 128×256 (solid black), (b) 128×256 (black), 64×128 (1 level, gray), 32×64 (2 levels, white) at 1.0 s (c) 32×64 (2 levels) with adaptive grid shown. The parameters used correspond to the ones listed in Table 2.

within 5% in comparison to the finest uniform grid (128×256). The adaptive grids chosen can thus be compared against the 128×256 uniform grid for efficiency gains.

The performance of the adaptive grids is compared against that of the 128×256 uniform grid in Table 5. It can be seen that the 32×64 adaptive grid is seven times faster and the 64×128 is about 3.4 times faster than the 128×256 uniform grid for similar accuracy as measured by interface shape (Fig. 7), and vapor volume and wall Nusselt number (Table 4). In addition to the speed up, the AMR efficiency is also computed for the adaptive grids. The AMR efficiency for the 32×64 adaptive grid is 52%. This compares with an AMR efficiency of 61% obtained by Fuster et al. (2009) for a two dimensional solution of the instabilities produced in primary atomization.

In order to compare the time history of the space-averaged Nusselt number, Nu_{avg} , for the simulated film boiling, the most widely used correlations of Berenson (1961) and Klimenko (1981) and Klimenko and Shelepen (1982) have been used. Berenson has derived the correlation for laminar film boiling near minimum heat flux as a function of Gr , Pr and Ja as $Nu = 0.425(GrPr/Ja)^{1/4}$. Klimenko's correlation for laminar film boiling on a horizontal surface is also a function of Gr , Pr and Ja and is given as $Nu = 0.19(GrPr)^{1/3}f_{Ja}$. Here, $f_{Ja} = 0.89Ja^{-1/3}$ for $Ja < 0.71$ and $f_{Ja} = 1$ for $Ja \geq 0.71$. Fig. 8 compares the evolution of Nu_{avg} for different grids against these correlations. It is seen that the predictions of the simulated results agree well with the correlations, in particular with that of Klimenko, after the initial transients decay. The Nu number for this test case falls in the low Morton number range and settles down to what may be a steady value at longer times. Such behavior of the simulated Nu number has also been observed in the results presented by Juric and Tryggvason (1998). It is to be noted that the bubbles computed in this study do not readily get released. This is consistent with the conclusions of Esmarelli and Tryggvason (2004b) who note that at intermediate superheats ($0.064 < Ja < 2.13$) permanent vapor jets are formed with no bubble break off. While, the pinch off process can be facilitated with the presence of a second interface, as has been done in the test cases presented by Esmarelli and Tryggvason (2004a), full three-dimensional simulations are needed to properly capture the pinch off process.

A film boiling test case for a higher density ratio is also investigated. The dimensionless parameters for this test case are: $\rho_l/\rho_v = 488$, $\mu_l/\mu_v = 25.9$, $k_l/k_v = 10$, $c_l/c_v = 1$, $Pr_v = 0.82$, $Gr = 158$, $Mo = 7.53 \times 10^{-5}$. The density ratio being high, the vapor quickly fills the computational domain of size $\sim (\lambda_{d2}, 2\lambda_{d2})$ on a 64×128

Table 4

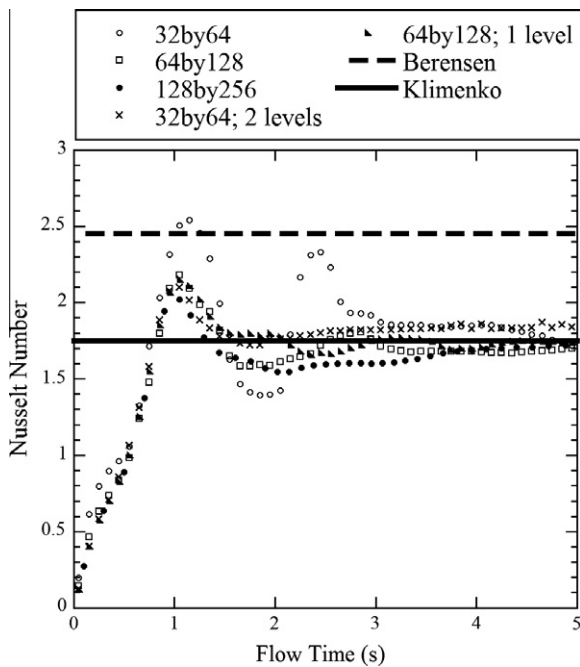
Film boiling: Grid convergence study in terms of vapor volume and Nusselt number at 1.0 s.

| | 32 × 64 | 64 × 128 | 128 × 256 | 32 × 64 (2 levels) | 64 × 128 (1 level) |
|--------------------------------|-----------|-----------|-----------|--------------------|--------------------|
| Vapor volume (m ³) | 0.2611395 | 0.2409050 | 0.2389070 | 0.2351367 | 0.2323785 |
| % Error (vol.) | 9.3 | 0.8 | – | –1.6 | –2.7 |
| <i>Nu</i> | 2.43 | 2.16 | 2.03 | 2.1 | 2.13 |
| % Error (<i>Nu</i>) | 19.7 | 6.4 | – | 3.4 | 4.9 |

Table 5

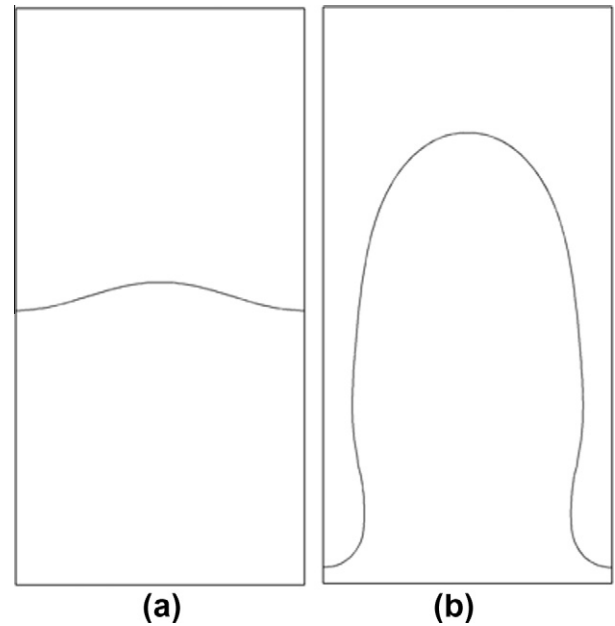
Film boiling: Efficiency improvement with the use of adaptive grid at 1.0 s.

| Parent grid size | Refinement level | Total number of cells (1.0 s) | Simulation time (s) | Speed up | AMR efficiency |
|------------------|------------------|-------------------------------|---------------------|----------|----------------|
| 128 × 512 | 0 | 65,536 | 9661 | 1 | – |
| 32 × 64 | 2 | 4952 | 1398 | 7 | 52.22 |
| 64 × 128 | 1 | 10,046 | 2866 | 3.4 | 21.67 |

**Fig. 8.** Evolution of Nu_{avg} for a single mode film boiling.

mesh. The initial perturbed interface, Fig. 9(a), is given by $y = y_c + A \cos(2\pi n_x/W)$. Here, $y_c = \lambda_{d2}$, $A = -0.05\lambda_{d2}$, $n_x = 1$ and $W = \lambda_{d2}$. The phase boundary at 0.213 s is shown in Fig. 9(b). As can be seen from the figure, the Taylor bubble has occupied most of the computational domain very quickly. The shape of the bubble is similar to the calculations done for the high density test case by Juric and Tryggvason (1998).

Having shown the accuracy and efficiency of the method to simulate two-dimensional film boiling, a test case for a full three dimensional film boiling simulation is presented. The relevant properties/parameters are the same as for the two-dimensional test case, listed in Table 2. A domain of size approximately $(1.3\lambda_{d3}, 1.3\lambda_{d3}, 1.3\lambda_{d3})$ is used for this test case with a parent grid resolution of $12 \times 12 \times 12$ with 4 levels of refinement. Only half the domain in x and z directions is used in the computational model with the use of symmetry conditions. The bottom surface is specified as a no-slip wall, while the top surface is specified as a pressure outlet (the static pressure is specified to be atmospheric with a temperature condition equal to the vapor saturation tem-

**Fig. 9.** A film boiling simulation at high density ratio, $\rho_l/\rho_v = 488$, $\mu_l/\mu_v = 25.9$, $k_l/k_v = 10$, $c_l/c_v = 1$, $Pr_v = 0.82$, $Gr = 158$, $Mo = 7.53 \times 10^{-5}$ (a) 0s, (b) 0.213s.

perature in the event backflow occurs). The interface cells and two rows of neighboring cells on either side of the interface are maintained at 4 levels of refinement. The interface is perturbed initially by

$$y = y_c + A_x(\cos(2\pi n_x/W_x) + \sin(\pi n_x/W_x)) + A_z(\cos(2\pi n_z/W_z) + \sin(\pi n_z/W_z)). \quad (21)$$

Here, $y_c = 0.125\lambda_{d3}$ is the unperturbed interface height, $A_x = -0.018\lambda_{d3}$ and $A_z = -0.018\lambda_{d3}$ are the maximum amplitudes of the perturbation in the x and z directions, the perturbation modes in x and z directions, n_x and n_z are chosen to be 2 and W_x and W_z are the length, and width of the domain, respectively.

Fig. 10 shows the (a) simulated volume fraction and (b) vertical velocity vectors with grid superimposed on x plane at $(x, y, z): 0.3, 0.0, 0.0$ at 1.36 s. A mushroom shaped vapor bubble evolves, as is seen from the figure. This test case demonstrates the robustness of the adaptive calculations to simulate full three-dimensional film boiling and provides an efficient and feasible platform to study multi-modal film boiling.

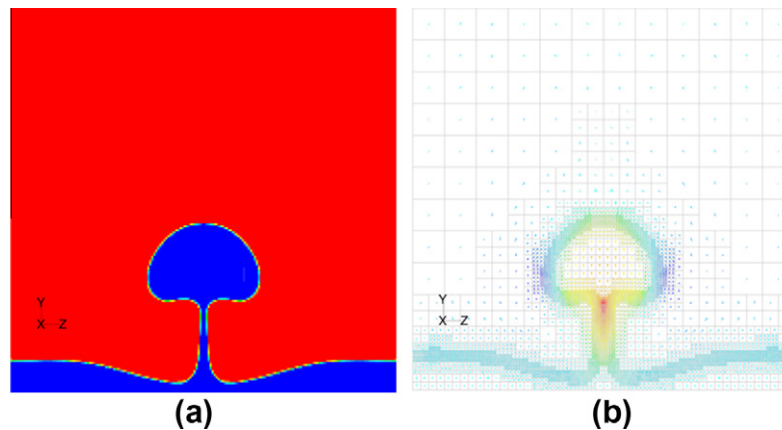


Fig. 10. Three-dimensional film boiling: (a) Contours of volume fraction and (b) vertical velocity vectors (blue–red: 0–2.2 m/s; grid superimposed, image reflected about symmetry boundary in z direction) on x plane at $(x, y, z): (0.3, 0.0, 0.0)$ at 1.36 s. (For interpretation of the references to color in this figure legend, the reader is referred to the web version of this article.)

4. Conclusions

Boiling flow simulations are conducted on adaptive octree grids. A phase change model is developed for use on grids which can adapt in space and time based on user specified criteria. The phase change calculations are not part of the standard FLUENT™ (6.3.26) solver. FLUENT™ only provides the users with the source terms for the mass, momentum and energy equations on a per cell basis, which can be specified by the user. In addition, FLUENT™ does not provide a direct means of specifying temperature boundary conditions at the interface. The calculations of the temperature gradients at the interface (both liquid and vapor temperature gradients), area of interface to cell volume ratio used to convert mass flux to cell volumetric source, mass source, momentum source and energy source are all done by user defined functions. In addition, the temperature boundary condition at the interface is specified with the aid of user-defined functions. Since, an octree grid is used for the test cases presented, grid adaption controls including updating memory allocation to the newly adapted grid at the beginning of each time step is also implemented by the user. The grid adaption function can mark the cells for adaption based on gradients of flow variables, proximity to the interface, and iso/gradient values of user defined memory locations. The use of octree grids provides an accurate and efficient platform to simulate complicated problems like boiling flows and makes computations of multi-mode film boiling in three dimensions feasible.

Test cases including Rayleigh–Taylor instability, Enright’s deformation test, bubble growth in uniform superheated liquid and film boiling were run to validate and demonstrate the capability and robustness of the technique. This sequence of test cases was chosen to demonstrate the critical parts of the technique including interface capturing with adaptivity, phase change on adaptive grids and finally instability growth with phase change (film boiling) on adaptive grids.

Film boiling simulations are conducted both on two and three dimensional adaptive grids. Two-dimensional test cases are used to demonstrate the spatial and temporal convergence and computational savings measured by speed up and AMR efficiency. The average computed wall Nusselt number agrees well with the widely accepted correlations of Berenson (1961), Klimenko (1981) and Klimenko and Shelepen (1982) for film boiling on a horizontal surface. A test case in three dimensions is also presented to demonstrate the robustness of the method to conduct boiling flow simulations without the use of ad-hoc models. This work opens the prospect of conducting more realistic multi-modal boiling flows, and problems of similar complexity, in an efficient manner.

Finally, for the test cases presented, the efficiency of the method as measured by the AMR efficiency is mostly in the range of 50–80%. Although this efficiency is a function of the nature and dimensionality of the problem, this range of efficiency obtained is comparable to those obtained in the simulations of primary jet atomization by Fuster et al. (2009). It is to be noted that these gains in efficiency are not optimized i.e., the grid distribution was not completely a function of gradients of flow and temperature fields. With the use of proper cost functions on grid adaptivity, the efficiency could be much higher and thus, for the test cases presented, the efficiency measure is conservative. In addition, use of adaptive techniques greatly reduces the size of the problem and thus, might not require large amounts of memory. This makes the solution of complex problems with wide range of scales feasible on desktop computers.

Acknowledgements

The authors wish to thank the Texas Learning and Computation Center (TLC²) for the use of computational facilities and their staff for their administrative support.

Appendix A. Supplementary material

Supplementary data associated with this article can be found, in the online version, at <http://dx.doi.org/10.1016/j.ijmultiphaseflow.2013.01.008>.

References

- Akhtar, M.W., 2011. Numerical Investigation of Vapor Bubble Interaction with a Superheated Wall. Department of Mechanical Engineering, University of Houston. PhD. Dissertation.
- Berenson, P.J., 1961. Film boiling heat transfer from a horizontal surface. *J. Heat Transfer* 83, 351–358.
- Brackbill, J.U., Kothe, D.B., Zemach, C., 1992. A continuum method for modeling surface-tension. *J. Comput. Phys.* 100, 335–354.
- Dergarabedian, P., 1960. The rate of growth of vapor bubbles in superheated water. *J. Appl. Mech.* 20, 537–545.
- Esmaeeli, A., Tryggvason, G., 2004a. Computations of film boiling. Part I: Numerical method. *Int. J. Heat Mass Transfer* 47, 5451–5461.
- Esmaeeli, A., Tryggvason, G., 2004b. Computations of film boiling. Part II: Multi-mode film boiling. *Int. J. Heat Mass Transfer* 47, 5463–5476.
- Florschuetz, L.W., Henry, C.L., Khan, A.R., 1969. Growth rates of free vapor bubbles in liquids at uniform superheats under normal and zero gravity conditions. *Int. J. Heat Mass Transfer* 12, 1465–1489.
- Francois, M., Cummins, S., Dendy, E., Kothe, D., Sicilian, J., Williams, M., 2006. A balanced-force algorithm for continuous and sharp interfacial surface tension models within a volume tracking framework. *J. Comput. Phys.* 213, 141–173.
- Fuster, D., Bagué, A., Boecc, T., Moyne, L.L., Leboissetier, A., Popinet, S., Ray, P., Scardovelli, R., Zaleski, S., 2009. Simulation of primary atomization with an

- octree adaptive mesh refinement and VOF method. *Int. J. Multiphase Flow* 35, 550–565.
- Issa, R.I., 1986. Solution of implicitly discretized fluid flow equations by operator splitting. *J. Comput. Phys.* 62, 40–65.
- Juric, D., Tryggvason, G., 1998. Computations of boiling flows. *Int. J. Multiphase Flow* 24, 387–410.
- Klimenko, V.V., 1981. Film boiling on a horizontal plate—new correlation. *Int. J. Heat Mass Transfer* 24, 69–79.
- Klimenko, V.V., Shelepen, A.G., 1982. Film boiling on a horizontal plate – a supplementary communications. *Int. J. Heat Mass Transfer* 25, 1611–1613.
- Kolev, N.I., 2002. *Multiphase Flow Dynamics 2: Thermal and Mechanical Interactions*. Springer-Verlag, Berlin, Heidelberg.
- Lao, Y.-J., Barry, R.E., Balzhiser, R.E., 1970. A study of film boiling on a horizontal plate. In: Paper B3.10, Fourth International Heat Transfer Conference, Paris, Versailles, “heat transfer 1970”, vol. V, Elsevier, Amsterdam.
- Lee, H.S., Merte, H.M., 1996. Spherical vapor bubble growth in uniformly superheated liquids. *Int. J. Heat Mass Transfer* 39, 2427–2447.
- Mikic, B.B., Rohsenow, W.M., Griffith, P., 1970. On bubble growth rates. *Int. J. Heat Mass Transfer* 13, 657–666.
- Nichita, B.A., 2010. An Improved CFD Tool to Simulate Adiabatic and Diabtic Two-Phase Flows. École Polytechnique Federale De Lausanne. PhD. Dissertation.
- Ozkan, F., Worner, M.W., Wenka, A., Soyhan, H.S., 2007. Critical evaluation of CFD codes for interfacial simulation of bubble-train flow in a narrow channel. *Int. J. Numer. Methods Fluids* 55, 537–564.
- Plesset, M.S., Zwick, S.A., 1954. The growth of vapor bubbles in superheated liquids. *J. Appl. Phys.* 25, 493–500.
- Popinet, S., 2009. An accurate adaptive solver for surface-tension-driven interfacial flows. *J. Comput. Phys.* 228, 5838–5866.
- Prosperetti, A., Plesset, M.S., 1978. Vapor bubble growth in a superheated liquid. *J. Fluid Mech.* 85, 349–368.
- Rayleigh, Lord, 1917. On the pressure developed in a liquid during the collapse of a spherical cavity. *Phil. Mag.* 34, 94–98.
- Renardy, Y.M., Renardy, M., 2002. PROST – a parabolic reconstruction of surface tension for the volume-of-fluid method. *J. Comput. Phys.* 183, 400–421.
- Rudman, M., 1997. Volume-tracking methods for interfacial flow calculations. *Int. J. Numer. Methods Fluids* 24, 671–691.
- Shin, S., Juric, D., 2002. Modeling three-dimensional multiphase flow using a level contour reconstruction method for front tracking without connectivity. *J. Comput. Phys.* 180, 427–470.
- Shin, S., Juric, D., 2009. A hybrid method for three-dimensional multiphase flows based on front tracking and level set techniques. *Int. J. Numer. Methods Fluids* 60, 753–778.
- Shin, S., Abdel-Khalik, S.I., Daru, V., Juric, D., 2005. Accurate representation of surface tension using the level contour reconstruction method. *J. Comput. Phys.* 203, 493–516.
- Shin, S., Yoon, I., Juric, D., 2011. The local front reconstruction method for direct simulation of two- and three-dimensional multiphase flows. *J. Comput. Phys.* 203, 493–516.
- Son, G., Dhir, V.K., 1997. Numerical simulation of saturated film boiling on a horizontal surface. *ASME J. Heat Transfer* 119, 525–533.
- Son, G., Dhir, V.K., 1998. Numerical simulation of film boiling near critical pressures with a level set method. *ASME J. Heat Transfer* 120, 183–192.
- Son, G., Dhir, V.K., Ramanujapu, N., 1999. Dynamics and heat transfer associated with a single bubble during nucleate boiling on a horizontal surface. *J. Heat Transfer* 121, 623–631.
- Sun, Y., Beckermann, C., 2004. Diffuse interface modeling of two-phase flows based on averaging: mass and momentum equations. *Physica D* 198, 281–308.
- Thulasidas, T.C., Abraham, M.A., Cerro, R.L., 1995. Bubble-train flow in capillaries of circular and square cross-section. *Chem. Eng. Sci.* 50, 183–199.
- Tryggvason, G., Bunner, B., Esmaeeli, A., Juric, D., Al-Rawahi, N., Tauber, W., Han, J., Nas, S., Jan, Y.J., 2001. A front tracking method for the computations of multiphase flow. *J. Comput. Phys.* 169, 708.
- Welch, W.J., Wilson, J., 2000. A volume of fluid based method for fluid flows with phase change. *J. Comput. Phys.* 160, 662–682.
- Zakerzadeh, S. A., 2008. “Applying dynamic contact angles to a three-dimensional VOF model” Department of Mechanical and Industrial Engineering, University of Toronto. PhD. Dissertation.